JOURNAL OF AIRCRAFT
Vol. 47, No. 3, May–June 2010

Hybrid Navier–Stokes/Free-Wake Method for Modeling Blade–Vortex Interactions

Byung-Young Min* and Lakshmi N. Sankar†
Georgia Institute of Technology, Atlanta, Georgia 30332-0150

DOI: 10.2514/1.46550

Techniques for accurate capturing of rotor blade–vortex-interaction phenomena are discussed. A number of algorithmic enhancements have been systematically examined, including geometric conservation law, refined metric and Jacobian computations, higher-order spatial and second-order temporal accuracy schemes, and embedded grids. The use of the geometric conservation law and refined metric computation were found to reduce nonphysical mass accumulation errors. These enhancements improve stability and accuracy of the higher-order schemes near far-field boundaries and in the vicinity of highly skewed cells. Embedded grids with an increased grid density were found to improve the predictions. It was also observed that the free-wake model (and, in particular, the determination of the trailing tip-vortex release point) plays a critical role in the blade–vortex-interaction prediction.

Nomenclature

α	=	angle of attack
C_d	=	airfoil drag coefficient
C_l	=	airfoil lift coefficient
C_m	=	airfoil pitching moment coefficient
C_n	=	airfoil normal-force coefficient
c	=	chord
E, F, G	=	flux vectors
J	=	grid Jacobian
k	=	reduced frequency
M	=	Mach number
P	=	pressure
Q	=	conservative variables vector, vortex identifier variable
q	=	flow properties
R	=	blade radius
r	=	blade radial location
t	=	nondimensionalized time
$\forall$	=	cell volume
w	=	weight factor
ξ, η, ζ	=	curvilinear coordinates
Ψ	=	azimuth angle

I. Introduction

THE flowfield around helicopter rotors is very complex. The rotor blades encounter wide variations in dynamic pressure (from incompressible flow to transonic flow), dynamic stall, and interaction with the self-generated wake. These effects contribute to loss in performance, noise, and vibrations. Because self-induced velocity of the vortex wake plays a dominant role in these phenomena, it is necessary to employ efficient and accurate techniques for capturing the tip-vortex strength and the temporal and spatial distribution of the vortex wake.

Full Navier–Stokes simulation of the vortical flow around a rotor requires large amount of grid points, especially for an accurate modeling of blade–vortex-interaction (BVI) phenomena. The number of grid points may be reduced with an adaptive grid or an overset mesh, but the computational cost in terms of time and memory is still prohibitive for engineering calculations. On the other hand, vortex-fitting techniques (free-wake and prescribed-wake methods) that model the wake as vortex sheets, tip-vortex filaments, and point vortices do not adequately model close blade-vortex encounters.

An alternative to wake-capturing and free-wake methods is a hybrid method that combines the best features of vortex-capturing and vortex-fitting techniques. These are Navier–Stokes/free-wake methods, which solve the flow around the rotor using Reynolds-averaged Navier–Stokes equations while capturing the far wake using discrete free-wake models. Since only the near field is modeled using the computationally expensive Navier–Stokes solver, the computational domain is much smaller than that for a full Navier–Stokes simulation. These methods give reasonable load predictions [1] for steady level flight and hover. However, BVI prediction of the hybrid method on coarse grids is unsatisfactory to date [2].

A. Objectives of the Present Study

In this work, several enhancements to an existing hybrid method aimed at improving the BVI modeling capability are systematically implemented. The improvements are assessed by correlating the results against the measured data for a 40%-scale model of the BO-105 rotor tested in The Netherlands at the DNW German–Dutch Wind Tunnels. The resulting data set is commonly known as the HART-II test database [3,4].

II. Computational Method

GENCAS [2,5,6] is a general-purpose three-dimensional compressible Navier–Stokes solver that has been developed by the first author. This method has recently been enhanced with a free-wake method developed by the second author and his coworkers. This method includes third-order MUSCL for cell-interface reconstruction, Roe's flux-difference-splitting scheme [7] for the inviscid flux computation, second-order central difference for viscous flux, and first-order implicit scheme for time-marching. A two-equation kinetic eddy simulation turbulence model [8] was used for estimating the eddy viscosity. The code has been parallelized using message-passing interface libraries for improved throughput.

If the rotor is in steady flight, the solution is periodic in time. Therefore, in the hybrid approach, the time-consuming Navier–Stokes simulations are carried out only for a single blade, in a small region surrounding this reference blade (Fig. 1a). The wake structure behind this reference blade and those of the other blades is modeled using a free-wake model (Fig. 1b). Only the trailing vortices from the blade tips are modeled in this study. The vortex strength of the most

Presented as Paper 3860 at the 27th AIAA Applied Aerodynamics Conference, San Antonio, TX, 22–25 June 2009; received 29 July 2009; accepted for publication 26 December 2009.

*Graduate Research Assistant, School of Aerospace Engineering. Student Member AIAA.

†Regents' Professor and Associate Chair, School of Aerospace Engineering. Associate Fellow AIAA.

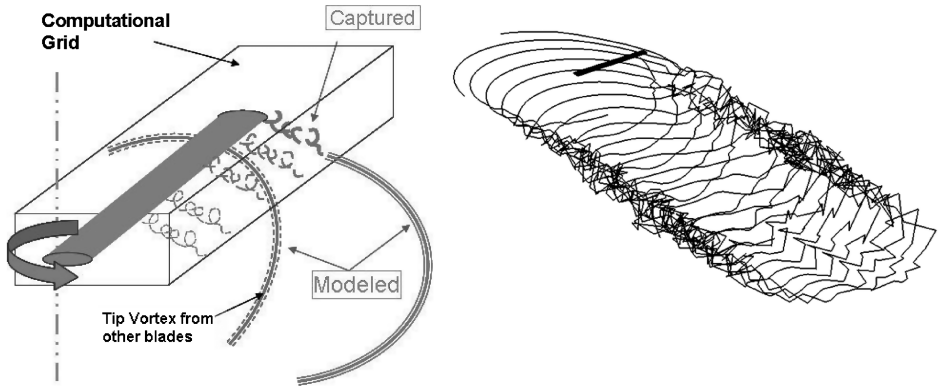

a) Illustration of the hybrid method b) Simulated free wake

Fig. 1 Schematic view of the hybrid method.

recently generated tip-vortex segment is assumed to be peak bound circulation at the instance the vortex segment is generated. The tip vortices are convected in space at the local velocity, calculated as the induced velocity due to all vortex filaments plus the freestream velocity. Biot–Savart law is used to compute the induced velocity. The induced velocities due to wake structure are also calculated at the outer surfaces of the Navier–Stokes computational domain at the inflow boundaries. This allows the vortices to reenter the computational domain. A detailed description of the wake model used in this study may be found in [9].

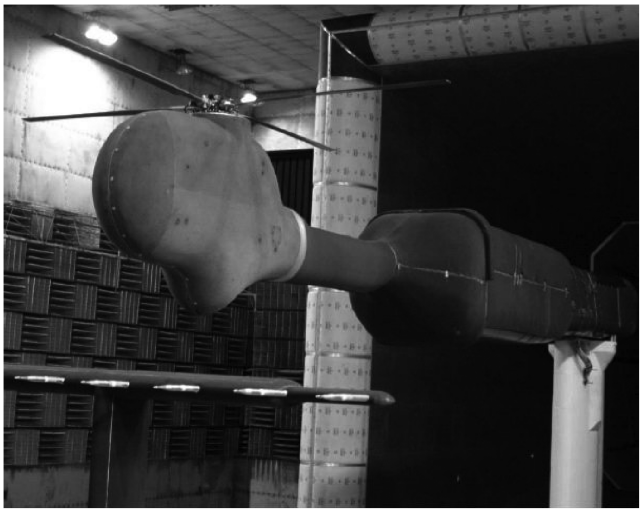

Fig. 2 HART-II model [3].

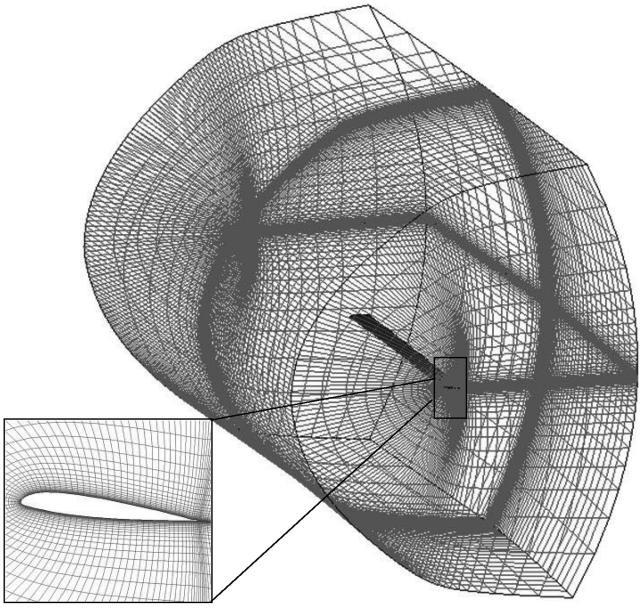

Fig. 3 Grid system for the reference blade (131 × 65 × 45).

A. Rotor Model and Simulation Method

Data from the HART-II program (Higher Harmonic Control Aeroacoustics Rotor Test) [3,4] were used in this study. The HART program is a common project undertaken by several international agencies to investigate the use of higher harmonic control for vibration and noise reduction. The rotor is a 40%-scale replica of the four-bladed hingeless BO-105 main rotor (Fig. 2). The rotor operates at 1040 rpm (corresponding to a hover tip Mach number of 0.638) at a nominal thrust coefficient of 0.00457. The shaft is tilted 5.3 deg aft in the present simulations. The available test data include the baseline descent case as well as higher harmonic control studies for minimum noise and minimum vibration. Since the present study is focused on improved BVI predictions, only the baseline case at an advance ratio 0.15 is discussed in this work.

The C-H grid is shown in Fig. 3 for the reference blade. The calculations were advanced in time for several revolutions until periodic behavior was achieved. A time-step sensitivity study with steps ranging from 0.01 and 0.25 deg azimuth per step was conducted, and a time step of 0.05 deg azimuth was found to give the best combination of accuracy and stability. Calculations were run for four full revolutions to establish a periodic solution. The wake geometry was updated once every 5 deg, with a new free-wake segment added once every 5 deg. The induced velocity at the outer surface of the Navier–Stokes domain was recalculated every time step.

The current computational method allows coupled computational fluid dynamics (CFD) and computational structural dynamics (CSD) analysis. To simplify the simulations, prescribed blade motions from Lim et. al [10] were used, obtained from an OVERFLOW2 CFD analysis loosely coupled to the CAMRAD-II comprehensive analysis.

III. Enhancements to the CFD Methodology for Capturing BVI Phenomena

To capture BVI phenomena accurately, several algorithmic enhancements were made. These are briefly described below.

A. Geometric Conservation Law

The Navier–Stokes equations may be written on a curvilinear coordinate system as follows:

$$\frac{\partial \bar{Q}}{\partial t}+\frac{\partial E}{\partial \xi}+\frac{\partial F}{\partial \eta}+\frac{\partial G}{\partial \zeta}=\frac{\partial E_v}{\partial \xi}+\frac{\partial F_v}{\partial \eta}+\frac{\partial G_v}{\partial \zeta} \tag{1}$$

where $\bar{Q}=(1/J)Q$. The current simulation involves aeroelastic deformations of the blade, which results in grid deformation and cell

volume changes for each of the cells at every time step. The Jacobian of the coordinate transformation, which is the inverse of the cell volume, is therefore a function of both time and space. The first term of the Eq. (1) becomes

$$\frac{\partial \bar{Q}}{\partial t} = \frac{\partial \forall Q}{\partial t} = \forall \frac{\partial Q}{\partial t} + Q\frac{\partial \forall}{\partial t} \tag{2}$$

The second term on the right side of Eq. (2) must be properly modeled to satisfy geometric conservation law (GCL) [11,12]. Neglecting this term is equivalent to placing an equivalent numerical source or sink in the flowfield. The magnitude of the second term on the right may be quite large far away from the rotor. These sources and sinks will affect the conservation of momentum and thus the conservation of vorticity. To mitigate this error, a properly formulated GCL has been included in the present numerical method.

The differential form of the GCL term in the generalized coordinate system may be expressed as

$$\frac{\partial \forall}{\partial t} = -\left[\frac{\partial}{\partial \xi}\left(\frac{\xi_t}{J}\right) + \frac{\partial}{\partial \eta}\left(\frac{\eta_t}{J}\right) + \frac{\partial}{\partial \zeta}\left(\frac{\zeta_t}{J}\right)\right] \tag{3}$$

With RHS denoting right-hand side, rearranging Eq. (1) using Eqs. (2) and (3) results in the following governing equation:

$$\frac{1}{J}\frac{\partial Q}{\partial t} + \frac{\partial E}{\partial \xi} + \frac{\partial F}{\partial \eta} + \frac{\partial G}{\partial \zeta} = \frac{\partial E_v}{\partial \xi} + \frac{\partial F_v}{\partial \eta} + \frac{\partial G_v}{\partial \zeta} + \mathrm{RHS}_{\mathrm{GCL}} \tag{4}$$

where

$$\mathrm{RHS}_{\mathrm{GCL}} = Q\left[\frac{\partial}{\partial \xi}\left(\frac{\xi_t}{J}\right) + \frac{\partial}{\partial \eta}\left(\frac{\eta_t}{J}\right) + \frac{\partial}{\partial \zeta}\left(\frac{\zeta_t}{J}\right)\right]$$

This term has been implemented in the present hybrid analysis.

B. Coordinate Transformation Jacobian and Metric Calculation

The errors associated with the computation of the Jacobians (the inverse of the cell volume) and metrics (which represent surface areas of the cell) may produce additional numerical sources or sinks. This error may be small and safely neglected if the cell size is small or the grid is nearly orthogonal. However, the error may not be negligible in the far field, where the grid is coarse and skewed. The errors in the calculation of cell volumes and cell-face areas may become even more significant if a disturbance such as an entering vortex is introduced at the far field.

An effort has made to refine the calculation of the Jacobian and associated metrics of transformation as follows. For every cell, the node-centered hexahedron is split into eight subhexahedra, as shown in Fig. 4a. Each of the hexahedra is further split into six tetrahedra (Fig. 4b). The volume of a node-centered cell is computed using Eq. (5):

$$\forall = \sum_{m=1}^{8}\sum_{l=1}^{6} \forall_{\mathrm{tedrahedron}_l} \tag{5}$$

where $\forall_{\mathrm{tetrahedron}} = \left|\frac{1}{6}\mathbf{a}\cdot(\mathbf{b}\times\mathbf{c})\right|$ and $J = 1/\forall$.

Figure 5 illustrates the procedure for computing the cell-face areas. As shown in Fig. 5a, conventional approaches for area computations using the four points may introduce significant errors on a highly skewed grid. To mitigate these errors, the surface area is expressed in the present work as the sum of four smaller areas, as shown in Fig. 5b.

C. Seventh-Order Weighted Essentially Nonoscillatory Scheme

A spatially-higher-order scheme is used to reduce artificial viscosity. The weighted essentially nonoscillatory (WENO) scheme introduced by Shu [13,14] is used, which is a cell-interface reconstruction scheme developed from ENO (essentially non-oscillatory) scheme for inviscid flux calculation. The WENO scheme uses all available combination of stencils, with nonlinear weighting factors, to achieve a high-order nonoscillatory interpolation of the flow properties at cell faces. The conventional ENO scheme, in contrast, uses only one combination of stencils out of many possible candidates. The seventh-order WENO scheme used in the present work employs a weighted average of cell-interface values, computed using four different combinations of seven points (Fig. 6), as shown in Eq. (6):

$$\begin{aligned} q_L &= w_L^{(1)}\hat{q}_{i+1/2}^{(1)} + w_L^{(2)}\hat{q}_{i+1/2}^{(2)} + w_L^{(3)}\hat{q}_{i+1/2}^{(3)} + w_L^{(4)}\hat{q}_{i+1/2}^{(4)} \\ q_R &= w_R^{(1)}\tilde{q}_{i+1/2}^{(1)} + w_R^{(2)}\tilde{q}_{i+1/2}^{(2)} + w_R^{(3)}\tilde{q}_{i+1/2}^{(3)} + w_R^{(4)}\tilde{q}_{i+1/2}^{(4)} \end{aligned} \tag{6}$$

where

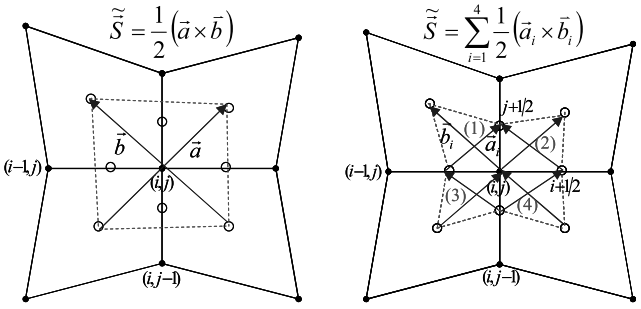

a) Conventional single quadrangle model **b) Refined interface area**

Fig. 5 Surface vector computation.

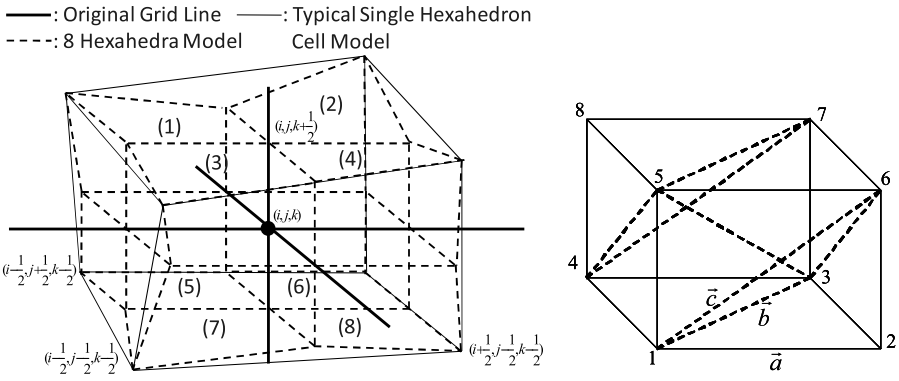

a) A node-centered cell split into 8 hexahedra on a skewed grid **b) A hexahedron split into 6 tetrahedra**

Fig. 4 Cell split.

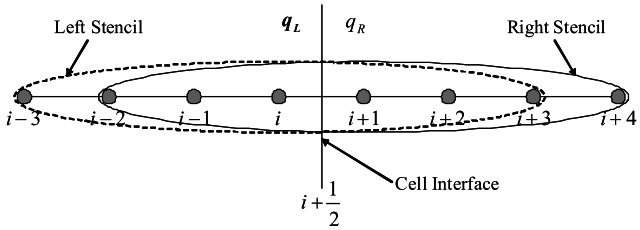

Fig. 6 Stencils used in seventh-order WENO scheme.

$$\begin{cases} \hat{q}^{(j)}_{i+1/2} = f(q_{i-j+1}, q_{i-j+2}, q_{i-j+3}, q_{i-j+4}) \\ \tilde{q}^{(j)}_{i+1/2} = f(q_{i+j}, q_{i+j-1}, q_{i+j-2}, q_{i+j-3}) \end{cases}$$

The weights depend on smoothness of the q values, such that the scheme prevents oscillation by proper selection of the weight. The reader is referred to [14] for details. The scheme gradually reduces to fifth-order WENO and third-order MUSCL interpolations near the boundaries.

D. Second-Order Time Accuracy with Newton Subiteration

In the baseline GENCAS analysis, an implicit two-point backward-difference scheme is used to advance the solution in time. This scheme is only first-order in time. To assess the effects of the temporal differencing scheme on the solutions, the analysis was enhanced with a second-order-accurate time-marching scheme with Newton subiterations. The governing equation in implicit form is given as follows:

$$\left[\frac{(1+\phi)}{J\Delta t} I + \delta_\xi A + \delta_\eta B + \delta_\zeta C\right]\Delta Q^m = \frac{\phi \Delta Q^{n-1}}{J^{n-1}\Delta t} - \frac{(1+\phi)(Q^m - Q^n)}{J\Delta t} + R(Q^m) \tag{7}$$

where

$$\Delta Q^m = Q^{m+1} - Q^m \qquad \Delta Q^{n-1} = Q^n - Q^{n-1} \qquad A = \frac{\partial E}{\partial Q}$$

$$B = \frac{\partial F}{\partial Q}, \qquad C = \frac{\partial G}{\partial Q} \qquad R(Q^m) = Q^m \mathrm{RHS}^m_{\mathrm{GCL}} + \mathrm{RHS}^m$$

If ϕ is 0, the discretization is first-order in time, and if ϕ is $\frac{1}{2}$, second-order accuracy in time is realized. The superscript m indicates the subiteration level. Use of Newton subiterations improves convergence and stability at the expense of computer time, because of the need to recompute the residual on the right-hand side of Eq. (7) after every iteration.

E. Embedded Grid

The artificial viscosity associated with the coarse grid at the outer boundary, as shown in Fig. 3, is one of the primary causes of dissipation of the tip-vortex strength. The artificial viscosity is of the order of Δ^n, where Δ is the grid spacing and n is determined by the order of spatial accuracy. To reduce artificial diffusion, the grid has to be fine enough in the region through which the vortex travels. For a structured grid, global refinement may increase the total number of computational cells to several millions. In the present study, a local refinement was therefore used; this was achieved with an embedded grid.

The embedded grid shown in Fig. 7 is nested inside a global grid. It is placed only in regions in which high gradients are expected. It is treated as another computational block, and the properties at the boundary points are obtained using linear interpolation from nearby global grid points. After every time step, the properties of the nodes within the global grid where the embedded grid is placed are updated using the properties on the embedded-grid block.

The embedded grid is regenerated every time step by refining the global grid after the global grid is translated in space (to account for blade rotation) and deformed (to account for elastic deformations, blade flapping, and pitching). Figure 7 illustrates a level-1 embedded grid.

IV. Results and Discussions

The algorithmic improvements discussed in the previous sections have been systematically assessed for their ability to model BVI phenomena accurately. The baseline hybrid method serves as the reference. This baseline method is third-order in space, first-order in

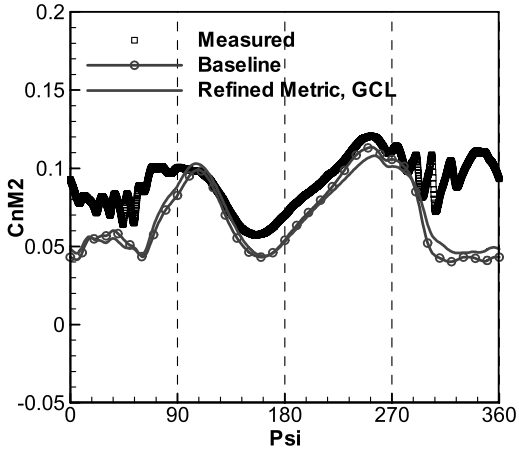

Fig. 8 Comparison of C_nM^2 at $r/R = 0.87$: baseline vs refined metric and GCL.

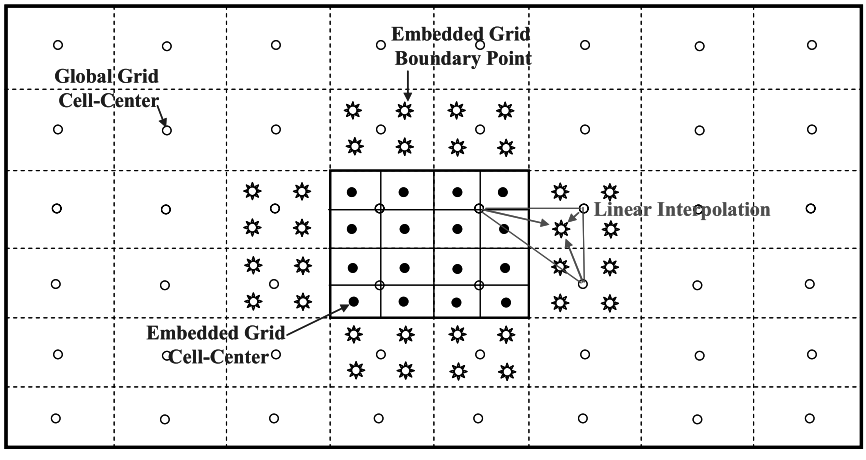

Fig. 7 Illustration of an embedded grid.

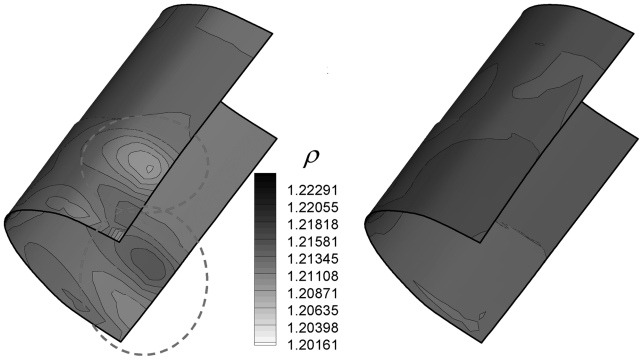

a) Baseline hybrid

b) Hybrid with GCL and refined metric

Fig. 9 Density contours at the outer surface.

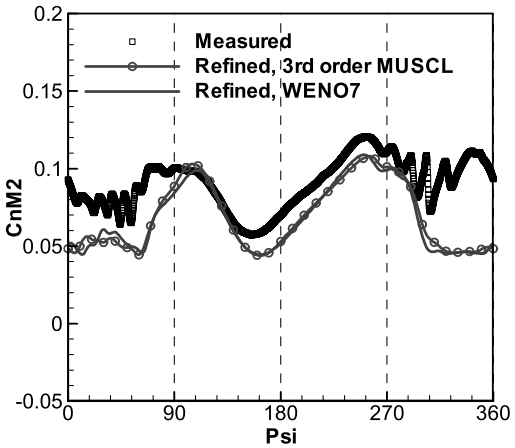

Fig. 10 Comparison of C_nM^2 at $r/R = 0.87$: third-order MUSCL vs seventh-order WENO and coarse grid.

time, with no GCL terms, and uses a conventional metric and Jacobian computation.

A. Effects of GCL, Refined Metric, and Jacobian

Figure 8 compares C_nM^2 of the baseline hybrid method with measured data. Results with the GCL case are also shown. First, it is observed that the baseline hybrid method predicts the low-frequency (3/rev) content of the loads reasonably, but completely misses high-frequency BVI load variation in the first and fourth quadrants. Even after the metric and Jacobian computation are refined and the GCL term is included, the BVI phenomena were not captured. This

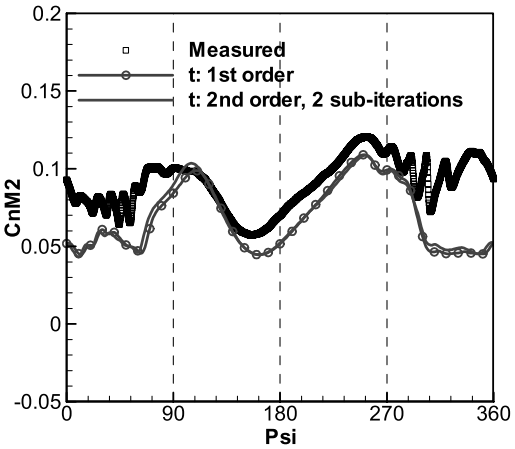

Fig. 11 Comparison of C_nM^2 at $r/R = 0.87$ for time accuracy: first-order vs second-order with two subiterations.

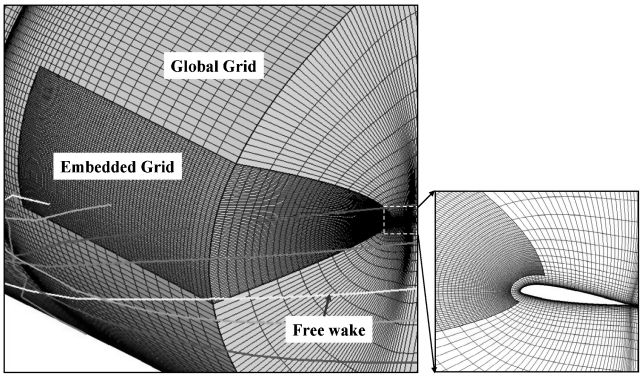

Fig. 12 Embedded grid.

indicates that the errors in volume and surface-area computations are not significant sources of the vortex dissipation in this particular instance. However, without the GCL term in the governing equation, a nonphysical mass accumulation or loss was observed at the outer surface, due to large cell deformation, as shown in Fig. 9. This nonphysical phenomenon was eliminated once GCL was applied.

B. Effects of Spatial and Time Accuracy

Figure 10 shows a comparison of normal-force history for the third-order and seventh-order schemes against test data. On the grid shown in Fig. 3, the use of the seventh-order scheme did not improve BVI prediction significantly. Although spatially-high-order schemes do have excellent accuracy and superior dissipation characteristics on uniform grids and fine curvilinear grids, unfortunately, these benefits do not always carry over to highly stretched or distorted grids. The magnitude of the truncation errors and numerical viscosity are of order Δ^n, where $n = 1, 3, 5, 7$ for first- through seventh-order WENO schemes. On highly stretched grids, Δ is large away from the body and higher-order schemes may have increased dissipation. It was observed that the seventh-order scheme was not stable with a conventional metric and Jacobian computation, especially near the blade tip region, where the grid is highly skewed. It appears that the inaccuracy of the conventional metric and Jacobian computation is large enough to destabilize the higher-order scheme on highly skewed grids. For this reason, the refined metric and grid Jacobian computations, along with GCL, were used in all of the subsequent studies below.

The effect of time accuracy on BVI prediction was minor when an azimuthal time step of 0.05 deg was used, as shown in Fig. 11. The second-order time scheme with Newton subiteration would allow larger time steps with added robustness and better convergence. However, since the computational time increases substantially with subiterations, and since the second-order temporal scheme does not

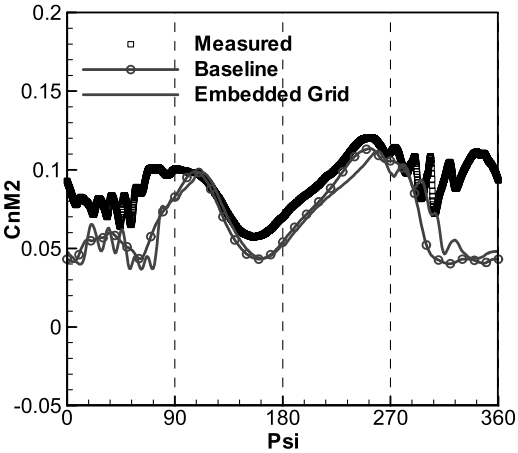

Fig. 13 Comparison of C_nM^2 at $r/R = 0.87$: baseline grid vs embedded grid.

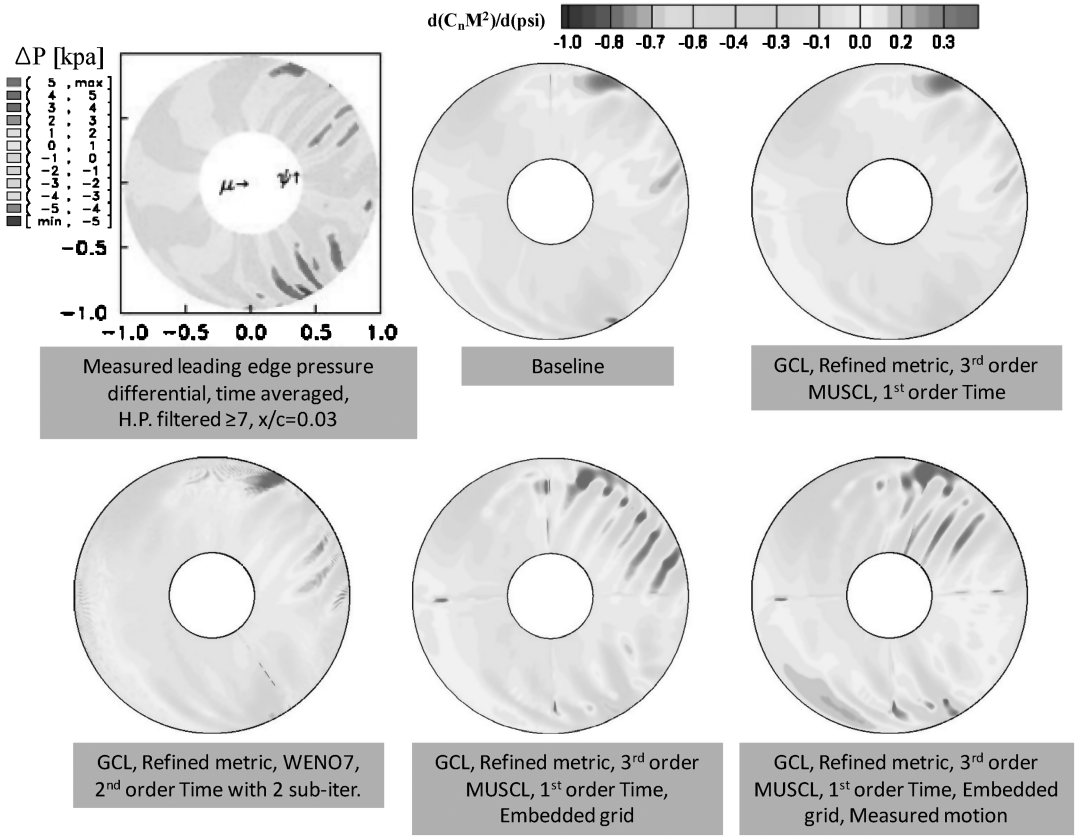

Fig. 14 Comparison of BVI pattern over the disk with measured data [4].

improve BVI prediction significantly, the subsequent studies used a first-order in time scheme without subiterations.

C. Effects of a Finer Grid Using an Embedded Grid

Figure 12 shows the embedded grid placed upstream of the blade in the region that captures entering wakes. The embedded grid was generated with a two-level split of the global grid; thus, 64 ($4 \times 4 \times 4$) cells were located inside one global cell. The computation was done using third-order MUSCL, first-order time accuracy with GCL, and refined metric and Jacobian computations.

The embedded-grid results shown on Fig. 13 more clearly show BVI encounters in the first and fourth quadrants. This confirms the earlier conjecture that the coarseness of the grid and the high attendant artificial viscosity is a significant contributor to tip-vortex dissipation and the inability of the baseline grid to resolve BVI events.

Contour plots of sectional loads, or even local pressures at representative locations on the blade, may be used to visually identify both the location and intensity of BVI events. In the HART-II experiment, leading-edge pressure difference was measured and plotted over the disk to identify the BVI. The high-pass-filtered measured pressure differential is shown in Fig. 14. For comparison, computed normal-force differentials from all of the studies described above are also shown. The baseline grid simulations do not pick up the distinct BVI patterns seen in experiments. On the other hand, simulations on the embedded grid show clear BVI patterns in the first quadrant, as in the measured data. However, the BVI events in the fourth quadrant were only weakly captured, compared with the experiment.

The conservation of tip vortices in the embedded grid is more clearly observed from Q isosurfaces in Fig. 15. Here, Q is defined as a balance between vorticity and strain rate [15]. Boundary-layer regions in which both vorticity and strain rate are high are excluded,

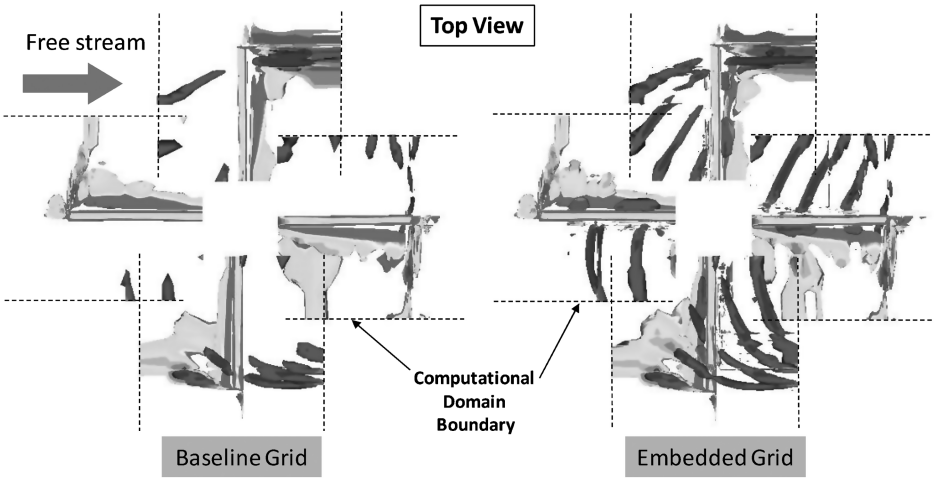

Fig. 15 Isosurfaces of Q at four azimuth positions, contoured by vorticity magnitude.

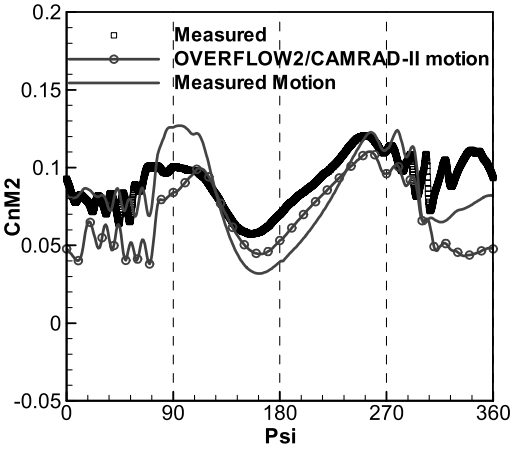

Fig. 16 Comparison of C_nM^2 at $r/R = 0.87$: OVERFLOW motion [10] vs measured motion [16].

and tip vortices are identified. It is clear that the baseline grid does not conserve the tip vortex once it is reintroduced in the computational domain. In particular, when the reference blade is located at the 0 deg azimuthal position, the entering tip vortices were quickly and artificially dissipated in the baseline grid. The embedded grid conserves the vortex strength relatively better, leading to an improved capture of BVI events in the first quadrant. A similar improvement in the capture of tip vortices and associated BVI events was also observed on the retreating side with embedded grids.

D. Effects of Measured Blade Motion

In all of the computations shown above, a motion file for the blade (which includes cyclic pitch and flap, along with the torsional and bending deformations) was used, obtained from OVERFLOW2 loosely coupled to a comprehensive analysis (CAMRAD-II). The cyclic pitch and collective pitch were from the internal trim done in the above CFD-CSD approach. It is observed in all of the results presented earlier that the mean value of the normal force is underpredicted and the loads over the fourth quadrant showed large deviation, especially around $\psi = 340$ deg.

To determine how much of these differences are attributable to the blade motion and the trim settings, a prescribed motion obtained from measured blade deflection data [16] was used. The deflection data of the reference (instrumented) blade was used in this study. The same algorithm options (first-order in time, third-order MUSCL, GCL, improved cell volume, and cell-area calculations) were used. An embedded grid was employed. The mode shapes of the blade were precomputed and the blade motion was defined such that the reconstructed data matched the measured deflection data in a least-squares sense. Up to three modes were needed for the flap, and two modes were used for lead lag and torsion.

Figure 16 indicates that the mean value of the load is shifted close to the experimental data, compared with earlier results using prescribed motions (e.g., Fig. 13). The low-frequency load prediction at the fourth quadrant has been improved and correlates better against measured data. However, some BVI events are not predicted well, and phase differences between computed and measured air loads exist. A main contributor to these BVI phase and

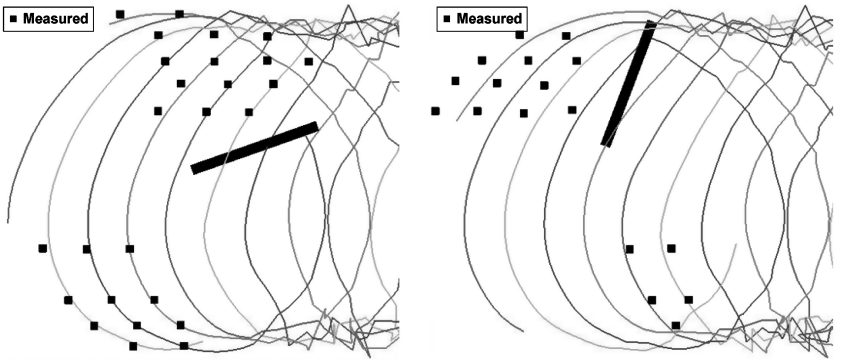

a) $\psi = 20^\circ$ **b)** $\psi = 70^\circ$

Fig. 17 Tip-vortex geometry, top view.

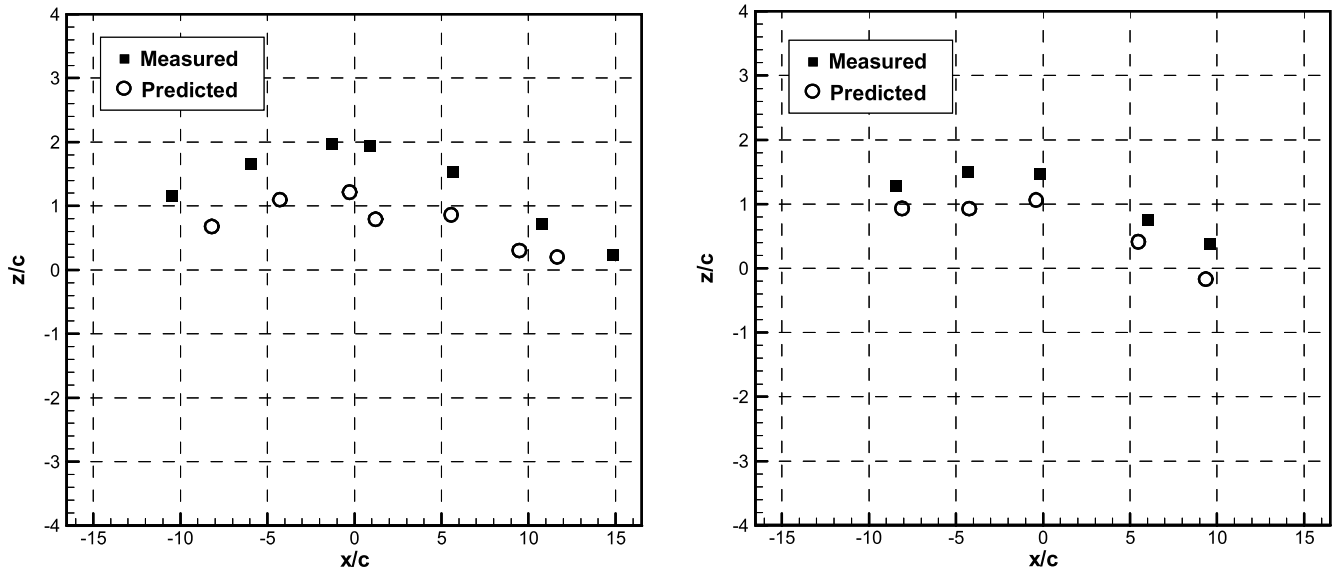

a) y=1.4 m (Advancing side) **b) y=-1.4 m (Retreating side)**

Fig. 18 Tip vortex, side view.

strength deviations is the free-wake trajectory, as shown in Figs. 17 and 18. From the top view, the wake position at the advancing side, especially over the second quadrant, shows a relatively poor correlation with test data. From Fig. 17b, it is shown that the tip-vortex shedding point is located more toward the outboard near the tip than that in the predictions. The current predictions used the peak-bound-circulation radial location as the position at which the free-wake was released into the flow. The vertical position of the tip vortex was also underpredicted. The wake trajectory prediction of the free wake and the estimates of the radial location at which the trailing tip vortices are released should be improved for a more accurate BVI prediction.

A further reason for the discrepancy is the pressure sensor instrumentation that modifies the dynamic characteristics of the reference blade, compared with the other three uninstrumented blades on this four-bladed system. Reference [17] compared the results using four different blade motions and showed an overshoot at around the 90 deg azimuth angle, similar to that in Fig. 16 for the reference blade (which was instrumented), whereas the overshoot was absent for other blades.

V. Conclusions

Several algorithmic improvements have been examined to improve BVI prediction capability of a Navier–Stokes/free-wake hybrid method. These include addition of a geometric conservation law term, refined grid metric and Jacobian computations, higher-order schemes in space and time, an embedded grid, and measured blade-motion data. The following conclusions are made.

1) The geometric conservation law and refined metric computation did not directly improve BVI prediction. However, errors (non-physical mass accumulation) due to numerical cell volume changes were eliminated with the use of GCL.

2) The use of refined grid metrics and Jacobians reduced numerical errors on highly skewed cells and allowed high-order schemes to be used in a stable, robust manner.

3) The seventh-order WENO scheme did not improve BVI prediction on the present coarse grids. However, improvements should be possible with a fine grid.

4) A second-order time scheme with Newton subiteration allows larger time steps with improved local convergence, but the effect of this enhancement on the BVI prediction was minor.

5) With an adequately refined embedded grid, BVI phenomena were better captured.

6) The mean normal-force and low-frequency loads are better predicted if a measured blade motion is used instead of OVERFLOW2/CAMRAD-II motion.

7) Comparison of the computed and measured tip-vortex trajectories showed large differences between predictions and measurements. Additional work is needed on algorithms that accurately determine where the tip vortices are released on the blade.

References

[1] Rajmohan, N., Sankar, L. N., Bauchau, O., Makinen, S. M., Egolf, T. A., and Charles, B. D., "Application of Hybrid Methodology to Rotors in Steady and Maneuvering Flight," *American Helicopter Society 64th Annual Forum* [CD-ROM], AHS International, Alexandria, VA, 2008.

[2] Min, B. Y., Sankar, L. N., and Yu, Y. H., "Computational Studies of the Effects of Gurney Flaps on the Autorotative Performance of Rotors in Descent Flight," *Proceedings of the AHS Aeromechanics Specialists Meeting* [CD-ROM], AHS International, Alexandria, VA, Jan. 2008.

[3] Yu, Y. H., Tung, C., van der Wall, B. G., Pausder, H., Burley, C., Brooks, T., Beaumier, P., Delrieux, Y., Mercker, E., and Pengel, K., "The HART-II Test: Rotor Wakes and Aeroacoustics with Higher-Harmonic Pitch Control (HHC) Inputs-The Joint German/French/Dutch/US Project," *American Helicopter Society 58th Annual Forum* [CD-ROM], AHS International, Alexandria, VA, June 2002.

[4] van der Wall, B. G., and Burley, C. L., "2nd HHC Aeroacoustic Rotor Test (HART II)—Part II: Representative Results," DLR, German Aerospace Center, Rept. IB 111-2005/03, Braunschweig, Germany, 2005.

[5] Min, B. Y., Sankar, L. N., Rajmohan, N., and Prasad, J.V.R., "Computational Investigation of the Effects of Gurney Flap on the Forward Flight Characteristics of Helicopter Rotors," AIAA Paper 2008-6726, Aug. 2008.

[6] Min, B. Y., Lee, W., Englar, R., and Sankar, L. N., "Numerical Investigation of Circulation Control Airfoils," *Journal of Aircraft*, Vol. 46, No. 4, July–Aug. 2009, pp. 1403–1410. doi:10.2514/1.41638

[7] Roe, P. L., "Approximate Riemann Solvers, Parameter Vectors, and Difference Schemes," *Journal of Computational Physics*, Vol. 43, No. 2, 1981, pp. 357–372.

[8] Fang, Y., and Menon, S., "A Two-Equation Subgrid Model for Large-Eddy Simulation of High Reynolds Number Flows," AIAA Paper 2006-116, Jan. 2006.

[9] Yang, Z., "A Hybrid Flow Analysis for Rotors in Forward Flight," Ph. D. Dissertation, Georgia Inst. of Technology, School of Aerospace Engineering, Atlanta, 2001.

[10] Lim, J. W., Nygaard, T. A., Strawn, R., and Potsdam, M., "BVI Airload Prediction Using CFD/CSD Loose Coupling," *AHS 4th Vertical Lift Aircraft Design Conference* [CD-ROM], AHS International, Alexandria, VA, Jan. 2006.

[11] Vinokur, M., "An Analysis of Finite-Difference and Finite-Volume Formulations of Conservation Laws," *Journal of Computational Physics*, Vol. 81, No. 1, 1989, pp. 1–52. doi:10.1016/0021-9991(89)90063-6

[12] Nichols, R. H., and Heikkinen, B. D., "Validation of Implicit Algorithms for Unsteady Flows Including Moving and Deforming Grids," AIAA Paper 2005-683, Jan. 2005.

[13] Shu, C. W., "Essentially Nonoscillatory and Weighted Essentially Nonoscillatory Schemes for Hyperbolic Conservation Laws," *Advanced Numerical Approximation of Nonlinear Hyperbolic Equations*, Lecture Notes in Mathematics, Vol 1697, Springer, New York, 1998, pp. 325–432.

[14] Shu, C. W., "High Order ENO and WENO Schemes for Computational Fluid Dynamics," *High-Order Methods for Computational Physics*, Lecture Notes in Computational Science and Engineering, Vol. 9, Springer, New York, 1999, pp. 439–582.

[15] Jeong, J., and Hussain, F., "On the Identification of a Vortex," *Journal of Fluid Mechanics*, Vol. 285, 1995, pp. 69–94. doi:10.1017/S0022112095000462

[16] van der Wall, B. G., "Mode Identification and Data Synthesis of HART-II Blade Deflection Data," DLR, German Aerospace Center, Rept. IB-111-2007/28, Braunschweig, Germany, June 2007.

[17] Yang, C., and Aoyama, T., "Effect of Computation Parameters on BVI Noise Prediction Using HART II Motion Data," *34th European Rotorcraft Forum*, Liverpool, England, U.K., Sept. 2008.